Laser Repetitive Pulse Heating of Steel Surface: A Material Response to Thermal Loading

S. Z. Shuja

A. F. M. Arif

B. S. Yilbas

Department of Mechanical Engineering,
King Fahd University of Petroleum and Minerals,
Dhahran, Saudi Arabia

Laser repetitive pulse heating of the workpiece surfaces results in thermal stresses developed in the vicinity of the workpiece surface. In the present study, laser repetitive pulse heating with a gas assisting process is modelled. A two-dimensional axisymmetric case is considered and governing equations of heat transfer and flow are solved numerically using a control volume approach while stress equations are solved using the finite element method (FEM). In this analysis, a gas jet impinging onto the workpiece surface coaxially with the laser beam is considered. A low-Reynolds number $k - \varepsilon$ model is introduced to account for the turbulence. When computing the temperature and stress fields two repetitive pulse types and variable properties of workpiece, and gas jet are taken into account. Temperature predictions were discussed in a previous study. A stress field is examined at present. It is found that the radial stress component is compressive while its axial counterpart is tensile. The temporal behavior of the equivalent stress almost follows the temperature field in the workpiece. The pulse type 1 results in higher equivalent stress in the workpiece as compared to that corresponding to pulse type 2. [DOI: 10.1115/1.1463033]

1 Introduction

Lasers are used in industry because of their precision of operation and their suitability for rapid processing. In laser processing, a gas jet is introduced either to i) enhance the exothermic reaction, which provides extra energy for metal processing, or ii) to minimize the oxidation effect for non-metallic substrate processing. In both cases, the physical phenomena are complicated and require extensive experimental and/or model studies for process improvement. Considerable model studies were carried out in the past to explore the laser induced heating process with or without gas jet considerations [1–3]. Inverse solution of the heat-transfer equation for application to steel and aluminum alloy quenching was investigated by Archambault and Azim [4]. They indicated that the inverse solution to the problem gave better insight into the formation of the martensite zone. Ji and Wu [5] simulated the temperature field during laser forming of sheet metals using the finite element method. They validated their predictions with other numerical techniques. They argued that the modeling could be carried out easily by the use of finite element method as compared to other techniques. Analytical solution for time unsteady laser pulse heating of a semi-infinite solid was obtained by Yilbas [6]. He showed that the conditions necessary for thermal integration to occur require a minimum pulse rate of 100 kHz and in the limit the solution reduced to that obtained for a step input pulse. Analysis of heat conduction in deep penetration welding with a time modulated laser beam was studied by Simon et al. [7]. They indicated that the time modulation had insignificant effect on the heat affected zone. Diniz Neto and Lima [8] predicted the temperature profiles inside the workpiece for high intensity laser pulse. They discussed the applicability of the model for practical cases. The heat transfer analysis of laser processing with conduction limited case was investigated by Yilbas and Shuja [9]. They introduced the equilibrium time and distance for each material, which changed with heating time. Heat conduction in a moving semi-infinite solid subjected to pulsed laser irradiation was investigated by Modest and Abaikans [10]. They observed that for a continuous source the integral method agrees well with the exact solution because the diffusion speed is greater than 10. Heat flow simula-

tion of laser remelting with experimental validation was carried out by Hoadley et al. [11]. They indicated that the predictions for the melt pool dimensions agreed well with the experimental findings. Hector et al. [12] obtained an analytical solution for the mode locked laser heating. In the solution, they considered the surface source model and omitted absorption of the laser beam. They indicated that the parabolic solution was not valid for a picosecond heating pulse.

In some laser surface treatment processes, a gas jet impinging onto the surface coaxially with the laser beam is considered. The impinging gas, in general, shields the surface from the oxidation reactions. When modelling the impinging gas jet, a stagnation point flow with the turbulence effects should be considered. Several modelling studies for impinging gas jets are reported [13–15]. In general, two-equation and high order models are considered to account for the turbulence. Craft et al. [16] investigated the gas jet impingement by considering the various turbulence models. They indicated that the standard $k - \varepsilon$ model overpredicted the viscous dissipation in the region close to the stagnation point. Strahle et al. [17] studied a two-dimensional planar flow using a two-equation model for a variable density case. They showed that the predictions obtained from a low-Reynolds number turbulence model agreed well with the experimental findings. Shuja and Yilbas [18] studied gas-assisted laser repetitive pulsed heating of a steel surface. They used a low-Reynolds number model to account for the turbulence. Their findings agreed well with the experimental results. The effect of variable properties on the laser pulsative heating of surfaces was carried out by Shuja and Yilbas [19]. They introduced a two equation turbulence model when formulating the gas jet impingement. They indicated that the thermal integration for the repetitive pulses of high cooling periods was unlikely and the effect of gas jet velocity was not substantial on the resulting solid site temperature profiles.

The variation of temperature in the substrate during laser heating produces thermal stresses. Since the thermal stress generated is highly localized, in some cases it leads to microcracks, significant decrease in bending strength, etc. in this region. Considerable research studies on thermal stresses due to laser irradiation are reported [20–21]. A study of thermal stresses during laser quenching was carried out by Wang et al. [22]. They indicated that residual stresses were developed on the surface of a laser quenched workpiece, which improved the hardness of the material. Modest

---

[23] investigated transient elastic and viscoplastic thermal stresses during laser drilling of ceramics. In the analysis the viscosity of the ceramic was treated as temperature dependent. He indicated that the ceramic had softened near the ablation front. The distortion gap width and thermal stresses in laser welding of thin elastic plates were examined by Darin et al. [24]. They obtained analytical expressions from the mismatch and the stress tensor was obtained from the thermoelastic infinite plate in terms of a convolution integral. Thermoelasticity for a multilayer substrate irradiated by a laser beam was studied by Elperin and Rudin [25]. They investigated the stress problem analytically and indicated that the analytical solution could be used for predictions of failures in multilayer coating-substrate system. A plane stress model for fracture of ceramics during laser cutting was examined by Li and Shang [26]. They showed that the fracture initiation, resulted from a high energy density cutting condition, could be avoided. Laser induced thermal stresses on a steel surface for a one-dimensional case was investigated by Yilbas et al. [27]. They indicated that considerable high amplitude thermal stresses developed in the surface vicinity. In order to explore the physical phenomena, the modelling of heating and resulting thermal stresses in axisymmetric consideration was necessary.

In the present study, laser repetitive heating of a steel substrate with gas impingement is modelled. The governing equations of flow and heat conduction are solved numerically using a control volume approach. A low-Reynolds number $k - \varepsilon$ model is considered to account for the turbulence. A finite element method is used to predict the thermal stresses in the heated region. In the simulations, the repetitive laser pulses of two types are considered and the variable material properties are taken into account.

2 The Mathematical Model

2.1 Flow and Heat Conduction Equations. Figure 1 shows the schematic view of the heating process. A round jet is considered as impinging normally on to a flat plate and the laser heat source has a Gaussian power intensity distribution across the plate surface; therefore, the jet and heating conditions become axisymmetric. Consequently, the problem considered reduces to a two-dimensional case. The unsteady two-dimensional axisymmetric form of the continuity and the time-averaged Navier-Stokes equations need to be solved to obtain the flow field due to gas jet impingement. The continuity and momentum equations are:

$$\frac{\partial \rho}{\partial t} + \frac{\partial}{\partial x_i}(\rho U_i) = 0 \tag{1}$$

and

$$\frac{\partial}{\partial t}(\rho U_j) + \frac{\partial}{\partial x_i}(\rho U_i U_j) = -\frac{\partial p}{\partial x_j} + \frac{\partial}{\partial x_i}\left[(\mu_t + \mu)\frac{\partial U_j}{\partial x_i}\right] \tag{2}$$

where μ_t is the eddy viscosity which has to be specified by a turbulence model. The partial differential equation governing the transport of thermal energy has the form:

$$\frac{\partial T}{\partial t} + \frac{\partial}{\partial x_i}(U_i T) = \frac{\partial}{\partial x_i}\left[\left(\frac{\mu_t}{\mathrm{Pr}_t} + \frac{\mu}{\mathrm{Pr}}\right)\frac{\partial T}{\partial x_i}\right] \tag{3}$$

Low-Reynolds number $k - \varepsilon$ turbulence model: The turbulent viscosity, μ_t, can be defined using the low-Reynolds number $k - \varepsilon$ model of turbulence [28], i.e.:

$$\mu_t = C_\mu \rho k^2 / \varepsilon \tag{4}$$

where C_μ is an empirical constant and k is the turbulence kinetic energy which is

$$\frac{\partial}{\partial t}(\rho k) + \frac{\partial}{\partial x_i}(\rho U_i k) = \frac{\partial}{\partial x_i}\left[\left(\frac{\mu_t}{\mathrm{Pr}_k} + \mu\right)\frac{\partial k}{\partial x_i}\right] + G - \rho\varepsilon \tag{5}$$

ε is the energy dissipation which is defined as:

$$\frac{\partial}{\partial t}(\rho\varepsilon) + \frac{\partial}{\partial x_i}(\rho U_i \varepsilon) = \frac{\partial}{\partial x_i}\left[\left(\frac{\mu_t}{\mathrm{Pr}_\varepsilon} + \mu\right)\frac{\partial\varepsilon}{\partial x_i}\right] + \frac{\varepsilon}{k}(C_1 G - C_2\rho\varepsilon) \tag{6}$$

G represents the rate of generation of turbulent kinetic energy and $\rho\varepsilon$ is its destruction rate. G is given by:

$$G = \mu_t\left[\left(\frac{\partial U_i}{\partial x_j} + \frac{\partial U_j}{\partial x_i}\right)\frac{\partial U_i}{\partial x_j}\right] \tag{7}$$

The model contains six empirical constants which are assigned the values in Table 1:

The Lam-Bremhorst low-Reynolds number extension to the $k - \varepsilon$ model employs a transport equation for the total dissipation rate [29]. It differs from the standard high-Reynolds number model in that the empirical coefficients C_μ, C_1 and C_2 are multiplied respectively by the functions:

$$f_\mu = (1 - e^{-0.0165\,\mathrm{Re}_l})^2\left(1 + \frac{20.5}{\mathrm{Re}_t}\right)$$

$$f_1 = 1 + \left(\frac{0.05}{f_\mu}\right)^3$$

$$f_2 = 1 - e^{-\mathrm{Re}_t^2}$$

where $\mathrm{Re}_l = z_n\sqrt{k}/\nu_l$ and $\mathrm{Re}_t = k^2/\varepsilon\nu_l$; and z_n is the distance to the nearest wall. For high-turbulence Reynolds numbers, Re_l or Re_t, the functions f_μ, f_1 and f_2 multiplying the three constants tend to unity.

2.2 Boundary Conditions for Flow Equations. Laminar boundary conditions are set for the mean-flow variables, and the boundary conditions $k = 0$ and $d\epsilon/dz = 0$ are applied at the wall. This is because the kinetic energy generation at the wall is zero
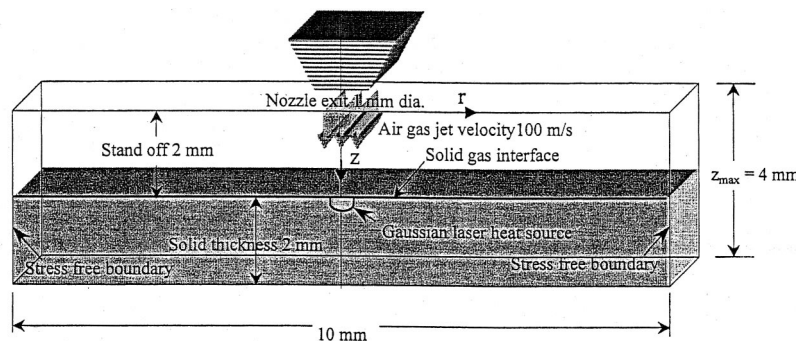

Fig. 1 Geometric arrangement of impinging gas and workpiece

Table 1   Constants in relation to turbulence model

C_μ	C_1	C_2	Pr_k	Pr_ε
0.09	1.44	1.92	1.00	1.00

due to the no-slip condition at the wall. Since the low-Reynolds number extension does not employ wall functions, and the flow field needs to be meshed into the laminar sublayer and down to the wall, the grid employed normal to the main flow direction needs to be distributed so as to give a high concentration of grid cells near the wall, with the wall-adjacent node positioned at $z^+ = \rho z u^* / \mu \lesssim 1.0$.

Inlet to control volume: $U_i =$ specified & $T =$ constant. The kinetic energy of turbulence is estimated according to some fraction of the square of the average inlet velocity: $k = \lambda \bar{u}^2$, where $\bar{u}$ is the average inlet velocity and λ is a fraction. The dissipation is calculated according to the equation: $\varepsilon = C_\mu k^{3/2}/bd$, where d is the inlet diameter. The values $\lambda = 0.03$ and $b = 0.005$ are commonly used and may vary slightly in the literature [30].

Outlet to control volume: It is considered that the flow extends over a sufficiently long domain; therefore, for any flow variable, at the exit section, ϕ the condition is: $\partial \phi / \partial x = 0$, where x is the arbitrary outlet direction [16].

Symmetry axis: The radial derivative of the variables is set to zero at the symmetry axis, i.e.: $\partial \phi / \partial r = 0$ and $V = 0$.

Solid fluid interface: The temperature at solid-gas interface is considered as the same, i.e.: $T_{w_{solid}} = T_{w_{gas}}$ and $K_{solid}(\partial T_{w_{solid}} / \partial z) = K_{gas}(\partial T_{w_{gas}} / \partial z)$

The unsteady heat conduction equation:

$$\frac{\partial}{\partial t}(c_p \rho T) = \frac{\partial}{\partial x_i}\left[K \frac{\partial T}{\partial x_i}\right] + S \tag{8}$$

where S is the unsteady spatially varying laser output power intensity distribution and is considered as Gaussian with $1/e$ points equal to 0.375 mm, i.e., the radius of the laser heated spot, from the center of the beam. Therefore, S is:

$$S = \frac{I_0}{\sqrt{2\pi a}}\exp\left(-\frac{r^2}{a^2}\right)\delta \exp(-\delta.z)f(t) \tag{9}$$

where $I_0 / \sqrt{2\pi a}\exp(-r^2/a^2)$ is the intensity distribution across the surface, $\exp(-\delta.z)$ is the absorption function, and $f(t)$ is the function which represents the time variation of the pulse shape. The

peak power intensity of the laser pulse (I_0) is 0.5×10^9 W/m^2 and the absorption depth (δ) of the substrate is 6.16×10^7 1/m.

Repetitive pulses: The repetitive pulses consist of a series of same intensity pulses having the same pulse length (1.5 ms) but different cooling periods (repetition rates). The cooling periods of pulse type 1 and 2 are 0.75 ms and 2.25 ms, respectively. The repetitive pulse profile employed is not rectangular shape but has rise and decay durations as given in the previous study [9]. The pulse rise and decay durations are kept constant for all the repetitive pulses for simplicity.

Boundary conditions for the heat conduction equation: At the front surface of the plate, the solid fluid interface, the continuity in temperature and heat flux is considered, which is similar to that corresponding to the gas side boundary condition at the solid fluid interface. Convection with a constant coefficient for still air is considered at the $z = z_{max}$ boundary for the rear side of the plate. It should be noted that no heat source is allocated at the rear side of the plate, i.e., the plate is heated from the top surface due to a laser source. The continuity of temperature between the solid and the gas is enforced at their interface; also far away from the laser source a constant temperature, $T = T_{amb}$, is assumed.

2.3 Variable Properties. Equation of state is used for the impinging gas and the specific heat capacity and thermal conductivity for both air and steel were considered as a function of temperature only. The temperature dependence of properties are given in [31] and tabulated in Table 2.

2.4 Calculation Procedure for Variables in Fluid and Solid. The calculation procedure for the temperature and the flow field is given in [9]. The SIMPLE (*Semi-Implicit Method for Pressure-Linked Equations*) algorithm [32,33] is used for the simulation of flow field. The grid used in the present calculations has 38×70 mesh points, which have a similar arrangement used in the previous study [9]. The grid independent test is satisfied and the results for space and time independence are shown in Fig. 2(*a*) and 2(*b*).

The governing equation for heat conduction in solid (Eq. (8)) can be written in the form of flow equations. Thus the discretization procedure leads algebraic equations of the form similar to flow equations with temperature T replacing the general variable. Although special care is taken to incorporate the spatially and time varying source, i.e., Eq. (9).

2.5 Thermal Stress Modelling. During laser material processing, the heating is localized and, therefore, a very large tem-

Table 2   Property Table

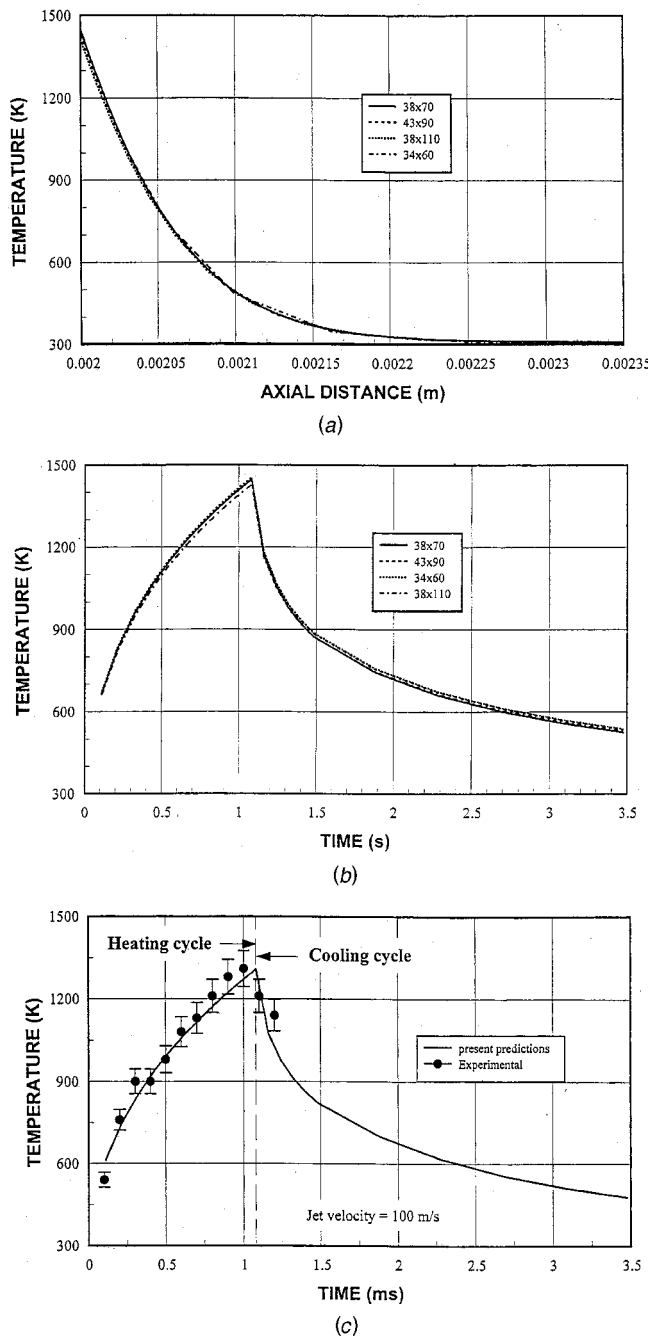| Property		Constant		Variable	
		Gas (Air)	Solid (Steel)	Gas (Air)	Solid (Steel)
Density	$\rho\ (kg/m^3)$	1.189	7836.0	p/RT	7836
Thermal Conductivity	$K\ (W/mK)$	0.02565	28.2	0.008103274 $+6.04893 \times 10^{-5}T$	64.102 $-0.04803T$ $+1.518 \times 10^{-5}T^2$
Specific heat capacity	$c_p\ (J/kgK)$	1005.0	969.0	$917 + 0.258T$ $+3.9804 \times 10^{-5}T^2$	$24.558 + 1.223T$ $-0.37693 \times 10^{-3}T^2$
Kinematic Viscosity	$\nu\ (m^2/s)$	1.544×10^{-5}		-0.494679×10^{-5} $+0.458394 \times 10^{-7}T$ $+0.80974 \times 10^{-10}T^2$	
Modulus of Elasticity	$E\ (GPa)$		11.7		$26.28 - 0.0922T$ $+2 \times 10^{-4}T^2$ $-2 \times 10^{-7}T^3$ $+6 \times 10^{-11}T^4$
Mean coeff. of thermal expansion	$\bar{\alpha}\ (\mu m/mK)$		217.96		$235.66 - 0.047T$ $-4 \times 10^{-5}T^2$
Poisson ratio	ν		0.3		

where $\{\boldsymbol{\epsilon}\}$ is the total strain vector and $\{\boldsymbol{\epsilon}^{\text{th}}\}$ is the thermal strain vector. Equation (10) may also be written as:

$$\{\boldsymbol{\epsilon}\}=[D]^{-1}\{\boldsymbol{\sigma}\}+\{\boldsymbol{\epsilon}^{\text{th}}\} \tag{11}$$

since the present case is axially symmetric, and the material is assumed to be isotropic, the above stress-strain relations can be written in cylindrical coordinates as:

$$\epsilon_{rr}=\frac{1}{E}[\sigma_{rr}-\upsilon(\sigma_{\theta\theta}+\sigma_{zz})]+\alpha\Delta T(r,z,t)$$

$$\epsilon_{\theta\theta}=\frac{1}{E}[\sigma_{\theta\theta}-\upsilon(\sigma_{rr}+\sigma_{zz})]+\alpha\Delta T(r,z,t)$$

$$\epsilon_{zz}=\frac{1}{E}[\sigma_{zz}-\upsilon(\sigma_{rr}+\sigma_{\theta\theta})]+\alpha\Delta T(r,z,t) \tag{12}$$

$$\epsilon_{rz}=\frac{1}{G}\sigma_{rz}$$

where E, υ, and α are the modulus of elasticity, poisson's ratio, and coefficient of thermal expansion, respectively. $\Delta T(r,z,t)$ represents the temperature rise at a point (r,z) at time$=t$ with respect to that at $t=0$ corresponding to a stress free condition. A typical component of thermal strain from Eq. (12) is:

$$\epsilon^{\text{th}}=\alpha\Delta T(r,z,t)=\alpha(T(r,z,t)-T_{\text{ref}}) \tag{13}$$

where T_{ref} is the reference temperature at $t=0$. If α is a function of temperature then Eq. (13) becomes:

$$\epsilon^{\text{th}}=\int_{T_{\text{ref}}}^{T}\alpha(T)dT \tag{14}$$

The present study uses a mean or weighted-average value of α, such that

$$\epsilon^{\text{th}}=\bar{\alpha}(T)(T-T_{\text{ref}}) \tag{15}$$

where $\bar{\alpha}(T)$ is the mean value of coefficient of thermal expansion and is given by:

$$\bar{\alpha}(T)=\frac{\int_{T_{\text{ref}}}^{T}\alpha(T)dT}{T(r,z,t)-T_{\text{ref}}} \tag{16}$$

The principal stresses $(\sigma_1,\sigma_2,\sigma_3)$ are calculated from the stress components by the cubic equation:

$$\begin{vmatrix} \sigma_{rr}-\sigma_p & \sigma_{r\theta} & \sigma_{rz} \\ \sigma_{r\theta} & \sigma_{\theta\theta}-\sigma_p & \sigma_{\theta z} \\ \sigma_{rz} & \sigma_{\theta z} & \sigma_{zz}-\sigma_p \end{vmatrix}=0$$

where σ_p is principal stress. The Von-Mises or equivalent stress, σ', is computed as

$$\sigma'=\sqrt{\frac{1}{2}[(\sigma_1-\sigma_2)^2+(\sigma_2-\sigma_3)^2+(\sigma_3-\sigma_1)^2]}$$

The equivalent stress is related to the equivalent strain through

$$\sigma'=E\epsilon'$$

where ϵ' is equivalent strain.

2.6 Calculation Procedure for Stresses. To develop a finite element procedure for stress computation, the standard displacement-based finite element method is used. The basis of this approach is the principle of virtual work, which states that the equilibrium of any body under loading requires that for any compatible small virtual displacements (which are zero at the boundary points and surfaces and corresponding to the components of displacements that are prescribed at those points and surfaces) imposed on the body in its state of equilibrium, the total internal virtual work or strain energy (δU) is equal to the total external

Fig. 2 (*a*) **The results of grid independence tests based on spatial distribution of temperature at time 1.08 ms. The solid surface is at 0.002 m.** (*b*) **The results of grid independence tests based on temporal variation of surface temperature at the center of the heated spot.** (*c*) **Temporal variation of surface temperature at the center of the heated spot.**

perature variation occurs over a small region. Owing to this temperature gradient, large thermal stresses are generated in the substrate, which can lead to the defects in the material such as the formation of cracks and the fractures in the material. The stress is related to strains by

$$\{\boldsymbol{\sigma}\}=[D]\{\boldsymbol{\epsilon}^e\} \tag{10}$$

where $\{\boldsymbol{\sigma}\}$ is the stress vector, and $[D]$ is the elasticity matrix.

$$\{\boldsymbol{\epsilon}^e\}=\{\boldsymbol{\epsilon}\}-\{\boldsymbol{\epsilon}^{\text{th}}\}$$

work due to the applied thermally induced loads (δV), i.e., $\delta U = \delta V$. For the static analysis of problems having linear geometry and thermo-elastic material behavior, one can derive the following equation using standard procedure [34].

$$\int_\forall (\{\boldsymbol{\delta\epsilon}\}^T[D]\{\boldsymbol{\epsilon}\} - \{\boldsymbol{\delta\epsilon}\}^T[D]\{\boldsymbol{\epsilon}^{\text{th}}\})d\forall$$

$$= \int_\forall \{\boldsymbol{\delta}\mathbf{U}\}^T\{\mathbf{f^B}\}d\forall + \int_\upsilon \{\boldsymbol{\delta}\mathbf{U_s}\}^T\{\mathbf{P}\}d\upsilon + \sum \{\boldsymbol{\delta\bar{U}}\}^T\{\mathbf{\bar{F}}\} \tag{17}$$

where

$\{\underline{\mathbf{f}}^B\}$=the applied body force, $\{\mathbf{P}\}$=the applied pressure vector, $\{\mathbf{\bar{F}}\}$=concentrated nodal forces to the element, $\{\boldsymbol{\delta}\mathbf{U}\}$=virtual displacement,

$\{\boldsymbol{\delta\bar{U}}\}$=virtual displacement of boundary nodes where concentrated load is prescribed.

$\{\boldsymbol{\delta\bar{U}_s}\}$=virtual displacement of boundary nodes where pressure is prescribed.

The strains may be related to the nodal displacement by:

$$\{\boldsymbol{\epsilon}\} = [B]\{\mathbf{\bar{U}}\} \tag{18}$$

where

$[B]$=strain displacement gradient matrix and $\{\mathbf{\bar{U}}\}$=nodal displacement vector.

The displacements within the elements are related to the nodal displacement by:

$$\{\mathbf{U}\} = [N]\{\mathbf{\bar{U}}\} \tag{19}$$

where $[N]$=matrix of shape (or interpolation) functions Equation (17) can be reduced to the following matrix form:

$$[K_e]\{\mathbf{\bar{U}}\} - \{\mathbf{F}^{\text{th}}\} = \{\mathbf{F}\}^b + \{\mathbf{F}\}^s + \{\mathbf{\bar{F}}\} \tag{20}$$

$[K_e] = \int_\forall [B]^T[D][B]d\forall$ =Element stiffness matrix
$\{\mathbf{F}^{\text{th}}\} = \int_\forall [B]^T[D][\in^{\text{th}}]d\forall$ =Element thermal load vector

where

$\{\mathbf{F}\}^b = \int_\forall [N]^T[f^B]d\forall$
$\{\mathbf{F}\}^s = \int_\upsilon [N_n]^T[P]d\upsilon$ =Element pressure vector
$[N_n]$=matrix of shape functions for normal displacement at the boundary surface

Assembly of element matrices and vectors of Eq. (20) yields

$$[K]\{\mathbf{\bar{d}}\} = \{\mathbf{\bar{R}}\}$$

where $[K]$, $\{\mathbf{\bar{d}}\}$ and $\{\mathbf{\bar{R}}\}$ are the global stiffness matrix, global nodal displacement vector, and global nodal load vector, respectively. Solution of the above set of simultaneous algebraic equations give unknown nodal displacements and reaction forces. Once displacement field is known due to temperature rise in the substrate, corresponding strain and stresses were calculated.

3 Validation

To validate the heat transfer model, the predictions for the surface temperature is compared with the experimental findings of the previous study [18] provided that the simulation is carried out for a single pulse laser heating. The pulse energy and the pulse length used in the simulation resemble the actual laser pulse employed in the experiment. Figure 2(c) shows the temporal variation of surface temperature predicted from the present study and its counterpart obtained from the experiment [18]. When comparing the predictions for temporal variation of surface temperature with the experimental results, it can be observed that both results are in good agreement. Small discrepancies between the results are due to the experimental uncertainty, which is 5 percent. Nevertheless, the discrepancies are negligibly small.

4 Results and Discussions

The simulations were carried out for two types of repetitive pulses. Since the predictions obtained for a temperature field were discussed in the previous study [9], the stress field predicted from the present study is presented.

Figure 3(a) shows the equivalent stress contours inside the workpiece at different times for pulse type 1. In the early heating time, the equivalent stress occurs close to the workpiece surface. As the heating progresses, the stress extends inside the material in the axial and radial directions provided that the radial direction extension is more pronounced as compared to axial direction due to spatial variation of laser power intensity. The high stress concentration occurs close to the surface and it attains the maximum value below the surface. In the case of the cooling cycle, the equivalent stress gradually decreases as the cooling progresses. The stress pattern changes more in the cooling cycle as compared to that corresponding to the heating cycle. In this case, a high stress concentration is developed below the surface and its location in the workpiece is almost independent of the cooling periods. Figure 3(b) shows the equivalent stress contours inside the workpiece for pulse type 2. The equivalent stress is highly concentrated in the surface region of the workpiece similar to the case for pulse type 1. As the heating progresses, the equivalent stress extends inside the surface. In the cooling cycle, the equivalent stress further extends inside the workpiece as the cooling progresses provided that its values reduce. The maximum stress occurs below the surface inside workpiece. Similar to pulse type 1, the stress contours differ considerably in the heating and cooling cycles. When comparing Figs. 3(a) and 3(b), the equivalent stress attains higher values for pulse type 1 as compared to pulse type 2. This is because of the temperature contours; i.e., a relatively steep temperature gradient is observed for pulse type 1 in the heating cycle [19].

Figure 4(a) shows the maximum temporal variation of the equivalent stress with its location inside the workpiece for pulse type 1. The maximum stress follows the temperature profile as shown in Fig. 4(b). In the early heating time, the rate of rise of maximum stress is considerable. As the pulse reaches its peak plateau, this rise reduces. The similar trend in the maximum stress is observed for the consecutive pulses. The amplitude of the maximum stress increases as the pulse repeats. This increase is due to the development of the temperature field in the workpiece with progressive heating time. In the cooling period of the repetitive pulses, the decay of the maximum stress is considerably high in the first half of the cooling period and the decay rate slows as the cooling period progresses. This is because of the temporal variation of temperature during the cooling period, i.e. the decay rate of temperature slows down towards the end of the cooling period, which is more pronounced in the first pulse. The location of the maximum stress in the substrate changes as the heating progresses. The location follows certain pattern for the consecutive pulses of two and three. In this case, during the heating cycle the maximum stress occurs below the surface with radial location at the center of the heated spot. In the cooling cycle, the location of maximum stress moves further inside the substrate while radial location changes from the irradiated spot center. Moreover, the location of maximum stress remains almost the same for the second and third of the consecutive pulses. This is again due to the temperature field developed inside the workpiece with time. In the case of first pulse type, the location of maximum stress does not follow a similar pattern, which is also observed for the other remaining consecutive pulses. In the heating cycle, the location of maximum stress moves inside the workpiece in the early rise of the pulse and it moves back to its initial location as the heating progresses. This may occur because the sudden rise of the temperature in the workpiece vicinity results in a considerably high temperature gradient in this region; in which case, the maximum stress moves slightly below its initial location. As the heating progresses, the thermal conduction enhances the temperature rise
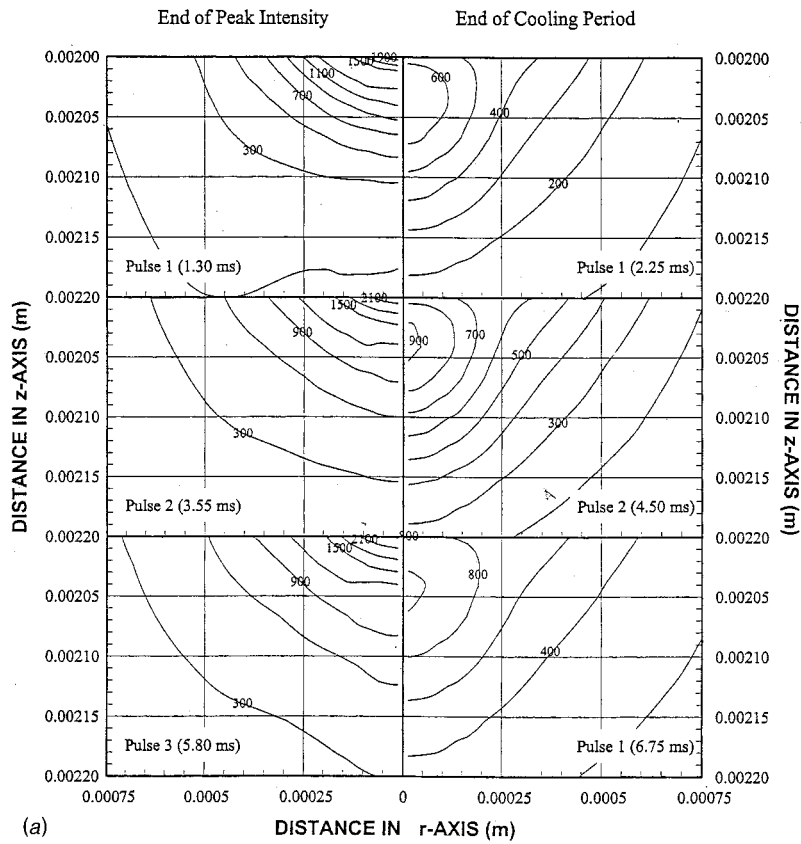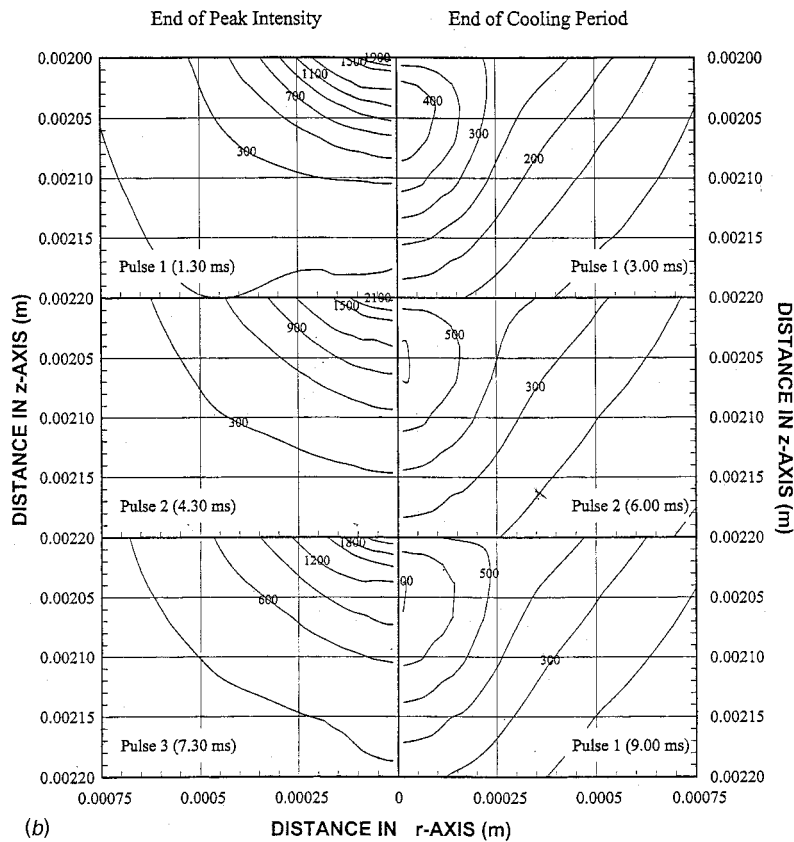
Fig. 3 (a) Equivalent stress contours (MPa) inside the substrate at different heating and cooling times for pulse type 1 (cooling period=0.5 pulse length). z=0.002 m is the free surface of the substrate. (b) Equivalent stress contours (MPa) inside the substrate at different heating and cooling times for pulse type 2 (cooling period=1.0 pulse length). z=0.002 m is the free surface of the substrate.
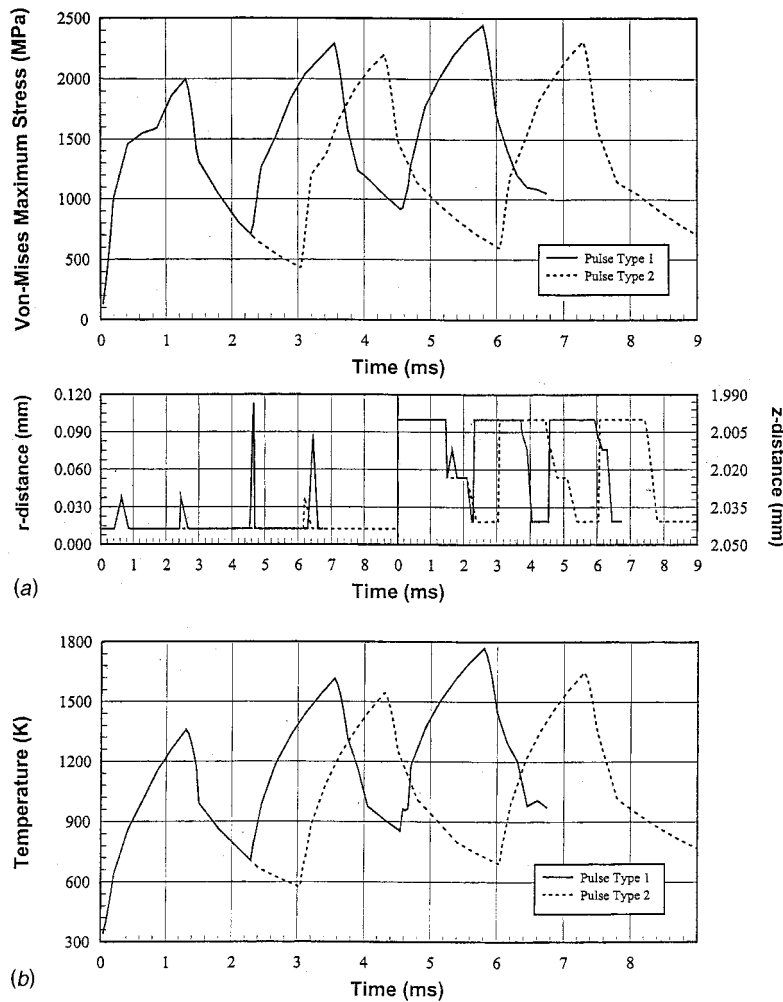
Fig. 4 (*a*) **Temporal variation of maximum equivalent stress and its respective locations along the radial and axial directions in the workpiece for pulse type 1 and 2.** (*b*) **Temporal variation of temperature where equivalent stress is mazimum for pulse type 1 and 2.**

below the surface and the temperature gradient in this region reduces, which leads to the change of maximum stress location in the workpiece. In the early cooling period, due to the rapid decay of the temperature after the first heating pulse, the location of the maximum stress changes more rapidly as compared to its counterparts corresponding to other consecutive pulses.

Similar arguments are valid for the maximum equivalent stress and its location for pulse type 2 as were made for pulse type 1. When comparing the maximum equivalent stress corresponding to pulse type 1 and 2, the maximum equivalent stress corresponding to pulse type 2 attains relatively lower values as compared to that corresponding to pulse type 1. Moreover, location of the maximum equivalent stress in the cooling cycle changes rapidly in the beginning of the cooling cycle and it gradually changes as the cooling period progresses for pulse type 2. The difference in the time variation of the location of maximum stress corresponding to pulse types 1 and 2 is because of the temporal variation of temperature difference for these pulses, i.e., the rise and decay rates of the temperature profiles are higher for the pulse type 1 as compared to that corresponding to the pulse type 2.

Figure 5 shows the temporal variation of the radial stress inside the workpiece at different axial locations and at the center of the heated spot for pulse type 1. The radial stress is compressive and it oscillates with time. This oscillation is due to repetitive pulse heating of the substrate. The radial stress reduces as the axial

distance from the surface reduces. This reduction amplifies as the axial distance from the surface increases beyond the point of 875 μm. In the first pulse of the consecutive pulses, the radial stress rapidly decreases in the first part of the heating cycle. However, the rate of decrease reduces as the heating progresses and it increases towards the end of the heating cycle. This is because of the temporal behavior of temperature, i.e., the rate of temperature rise reduces as the heating period progresses, which, in turn results in similar temporal behavior of radial stress. The rate of change of radial stress with time for all consecutive pulses are almost the same in the cooling cycle. Moreover, as the axial depth from the surface increases, the time corresponding to maximum radial stress shifts. This is because of the material response to the heating pulse; in this case, the temperature profiles in the radial direction extends into the substrate nonlinearly as the heating progresses [19]. The time rate of change of radial stress in the heating cycle is almost similar to its counter part in the cooling cycle with inverse sign. Consequently, this variation does not follow the similar variation observed for the temperature profiles as indicated in the previous study [19].

Figure 6 shows the temporal variation of axial stress at different axial locations for pulse type 1. The axial stress is zero at the free surface. As the depth from the surface increases, the axial stress oscillates with time similar to temperature oscillation provided that the stress is compressive during the cooling period. As the
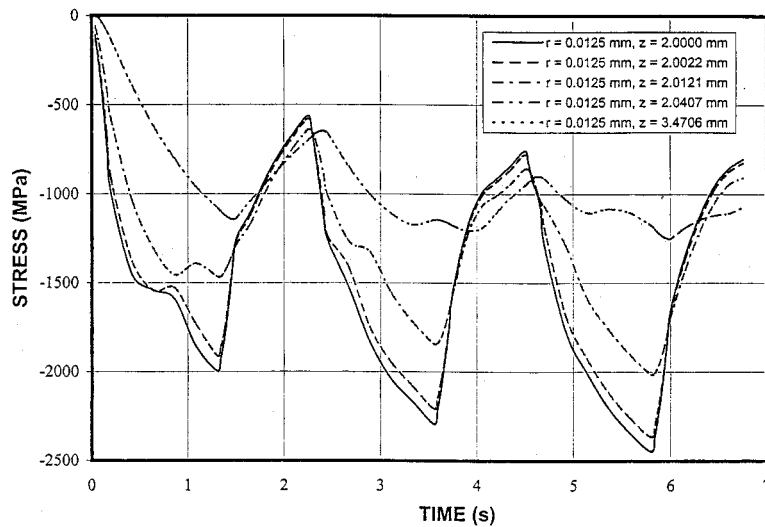
Fig. 5 Temporal variation of radial stress at different *z*-locations in the substrate for pulse type 1

depth from the surface increases further, axial stress increases stepwise with time, i.e., no oscillation in the stress is observed. This occurs because of the material response to repetitive pulses. In this case, at some depth below the surface, the conduction dominates the rapid internal energy gain of the substrate, since the absorption depth of the substrate is in the order of 10^{-7} m. Consequently, the pulsative temperature profile is replaced by the gradual increasing profile with time as discussed in the previous study [19]. Therefore, the axial stress profile increases gradually with time provided that the stress is tensile at this depth. Moreover, the magnitude of the axial stress is in the order of a couple of MPa, which is considerably small as compared to the magnitude of radial stress.

Figure 7 shows the temporal variation of the equivalent stress at different location in the workpiece and radial location is the center of the heated spot for pulse type 1. The maximum value of the equivalent stress occurs at the end of the heating cycle of each of the consecutive pulses and its value increases as the number of consecutive pulses increases. As the distance in the axial direction increases, the value of maximum equi-

valent stress reduces. The rise of the equivalent stress in the heating cycle is similar in the surface vicinity. As the depth in the axial direction from the surface increases the rise in the equivalent stress reduces. This is because of the temporal behavior of the temperature in the substrate; in which case, the temperature extends into the workpiece at a slow rate as the distance in the axial direction from the surface increases as depicted in the previous study [19]. This is because in the surface vicinity the energy absorbed from the laser irradiation enhances the internal energy gain and it increases as the heating cycle progresses. However, the increase of temperature in the substrate beyond the absorption depth occurs by heat conduction due to temperature gradient across the absorption zone and the region next to it. Consequently, the temperature rises at faster rate in the absorption depth as compared to the region next to it. The magnitude of equivalent stress is similar to that corresponding to radial stress components (Fig. 5). This is because the lower magnitude of axial stress component as compared to radial stress component.
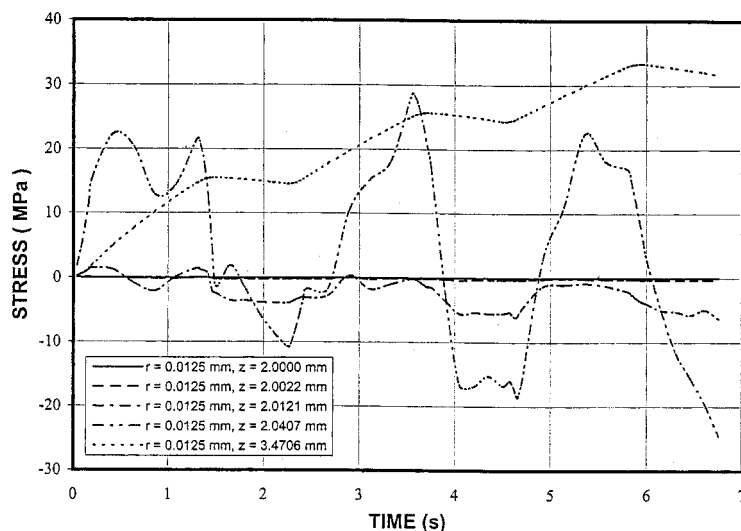

Fig. 6 Temporal variation of axial stress at different *z*-locations in the substrate for pulse type 1
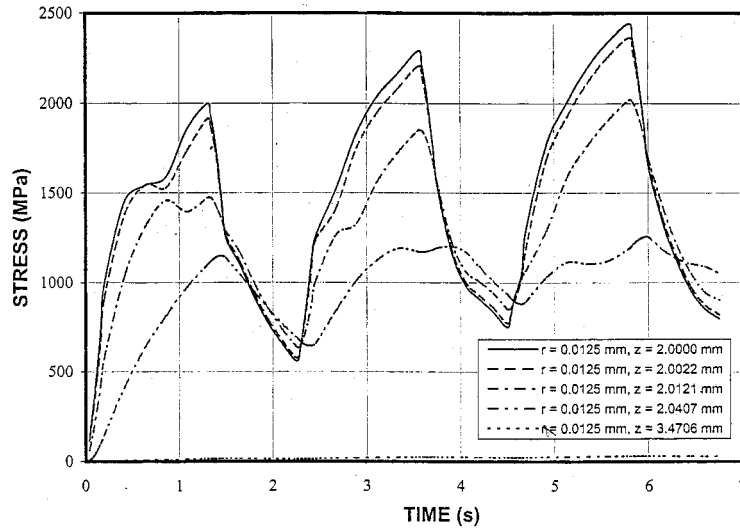
Fig. 7   Temporal variation of equivalent stress at different *z*-locations in the substrate for pulse type 1

5   Conclusions

The laser repetitive pulse heating of steel surface with a gas jet assisting process is modeled for variable properties cases. Two repetitive pulse types are considered. A two-dimensional axisymmetric heating model including gas jet impingement is introduced and solved numerically. A low-Reynolds number $k-\epsilon$ model is used to account for the turbulence. Since the temperature response of the workpiece was discussed in a previous study, the thermal stresses are the main concern in the present work. In general, the radial stress component is compressive while the axial component is found to be tensile. The temporal behavior of the equivalent stress follows almost the temperature field. The pulse type 1 results in a higher rate of stress development in the workpiece as compared to that corresponding to the pulse type 2. The specific conclusions derived from the present work may be listed as follows:

1 The equivalent stress contours extend inside the workpiece as the heating progresses. The stress pattern changes in the cooling cycle as compared to the heating cycle; in which case, the stress concentration is developed below the surface and its location is almost independent of the cooling periods. The pulse type affects the equivalent stress such that it attains higher values for pulse type 1.

2 The rise of the equivalent stress in the beginning of the heating cycle is considerable; however, as the heating progresses, this rise reduces. The maximum stress amplitude increases as the repetition of pulses increases. The decay rate of the maximum equivalent stress varies in the cooling period; in this case, the maximum stress reduces rapidly in the early part of the cooling period. This is more pronounced for the first pulse of the consecutive pulses.

3 The maximum stress location occurs below the surface with its radial location at the center of the heated spot in the heating cycle. In the cooling cycle, the location of the maximum stress moves further inside the workpiece as well as its location in the radial direction changes. However, the location remains the same as the pulse repetition progresses. Moreover, this location of maximum stress changes for different pulse types employed.

4 The radial stress is compressive and it varies with time. The rapid decay of the radial stress is observed for the depth of 875 μm and beyond from the surface. The temporal variation of the radial stress corresponding to different pulse types are almost similar provided that as the axial depth from the surface increases, the time corresponding to maximum radial stress shifts.

5 The equivalent stress attains its maximum at the end of the heating cycle of the consecutive pulses. The rise of the equivalent stress in the surface vicinity and at a depth below the surface is different; in this case, the rise of the equivalent stress reduces as the depth from the surface increases.

Acknowledgment

Nomenclature

a = Gaussian parameter
C_1, C_2, C_μ = coefficients in the $k-\varepsilon$ turbulence model
c_p = specific heat capacity, J/kgK
d = diameter of the nozzle, m
f_1, f_2, f_μ = coefficients in the low Reynolds no., $k-\varepsilon$ model
E = modulus of elasticity, MPa
G = rate of generation of k, W/m^3
I_0 = peak power intensity, W/m^2
k = turbulent kinetic energy, W/m^3
K = thermal conductivity, W/mK
p = pressure, Pa
Pr = variable Prandtl no. (function of temperature)
q = heat flux, W/m^2
Re = Reynolds no.
r = distance in the radial direction, m
S = unsteady spatially varying source (Eq. (8)), W/m^3
t = time, s
T = temperature, K
U = arbitrary velocity, m/s
V = radial velocity, m/s
W = axial velocity, m/s
x = arbitrary direction, m
z_n = distance to the nearest wall, m
z = distance in the axial direction, m
D = elasticity matrix
$\Delta T(r,z,t)$ = temperature rise at a point (r,z) at time$=t$ with respect to that at $t=0$
T_{ref} = reference temperature at $t=0$
$\{\mathbf{f}^B\}$ = the applied body force
$\{\mathbf{P}\}$ = the applied pressure vector

$\{\bar{\mathbf{F}}\}$ = concentrated nodal forces to the element

$\{\boldsymbol{\delta}\mathbf{U}\}$ = virtual displacement

$\{\boldsymbol{\delta}\mathbf{U_s}\}$ = virtual displacement on the boundary where pressure is prescribed

$\{\boldsymbol{\delta}\bar{\mathbf{U}}\}$ = virtual displacement of boundary nodes where concentrated load is prescribed

$[B]$ = strain displacement gradient matrix

$\{\bar{\mathbf{U}}\}$ = nodal displacement vector

$[N]$ = matrix of shape (or interpolation) functions

$[K_e] = \int_{\forall}[B]^T[D][B]d\forall$, element stiffness matrix

$\{\mathbf{F}^{th}\} = \int_{\forall}[B]^T[D][\epsilon^{th}]d\forall$, element thermal load vector

$\{\mathbf{F}\}^b = \int_{\forall}[N]^T[f^B]d\forall$, element applied body force vector

$\{\mathbf{F}\}^s = \int_{\upsilon}[N_n]^T[P]d\upsilon$, element pressure vector

$[N_n]$ = shape functions for normal displacement at the boundary surface

Greek

σ = stress vector, MPa

$\sigma_{\mathbf{p}}$ = principal stress, MPa

$\{\boldsymbol{\epsilon}\}$ = total strain vector

$\{\boldsymbol{\epsilon}^{th}\}$ = thermal strain vector

ϵ' = equivalent strain

α = Coefficient of thermal expansion

υ = Poisson's ratio

Γ = diffusion coefficient

δ = absorption coefficient, 1/m

ε = energy dissipation, W/kg

λ = thermal conductivity, W/mK

κ = turbulence intensity

μ = variable dynamic viscosity (function of temperature for laminar), N s/m^2

μ_e = effective viscosity ($\mu_l + \mu_t$), N s/m^2

ν = variable kinematic viscosity (function of temperature for laminar), m^2/s

ρ = density (function of temperature and pressure for gas), kg/m^3

Φ = viscous dissipation, W/m^3

ϕ = arbitrary variable

subscript

amb = ambient

i,j = arbitrary direction

jet = conditions at jet inlet

l = laminar

max = maximum

t = turbulent

References

[1] Ready, J. F., 1965, "Effects due to Absorption of Laser Radiation," J. Appl. Phys., **36**, pp. 462–470.

[2] Schultz, W., Becher, D., Frank, J., Kennerling, K., and Herziger, G., 1993, "Heat Conduction Losses in Laser Cutting of Metals," J. Phys. D, **26**, pp. 1357–1363.

[3] O'Neill, W., and Steen, W. M., 1995, "A Three Dimensional Analysis of Gas Entrainment Operating During the Laser Cutting Process," J. Phys. D, **28**, pp. 12–18.

[4] Archombault, P., and Azim, A., 1995, "Inverse Solution of the Heat-Transfer Equation: Application to Steel and Aluminum Alloy Quenching," J. Mater. Eng. Perform., **4**, pp. 730–736.

[5] Ji, Z., and Wu, S., 1998, "FEM Simulation of the Temperature Field During the Laser Forming of Sheet Metal," J. Mater. Process. Technol., **74**, pp. 89–95.

[6] Yilbas, B. S., 1996, "Analytical Solution for Time Unsteady Laser Pulse Heating of Semi-infinite Solid," Int. J. Mech. Sci., **30**, pp. 671–682.

[7] Diniz Neto, O., and Lima, C. A. J., 1994, "Non-Linear Three Dimensional Temperature Profiles in Pulsed Laser Heated Solids," J. Phys. D, **27**, pp. 1795–1804.

[8] Simon, G., Gratzke, U., and Kroos, J., 1993, "Analysis of Heat Conduction in Deep Penetration Welding With a Time-Modulated Laser Pulse," J. Phys. D, **26**, pp. 862–869.

[9] Yilbas, B. S., and Shuja, S. Z., 1997, "Heat Transfer Analysis of Laser Heated Surfaces-Conduction Limited Case," Appl. Surf. Sci., **108**, pp. 167–175.

[10] Modest, M. F., and Aboikans, H., 1986, "Heat Conduction in a Moving Semi-infinite Solid Subjected to Pulsed Laser Irradiation," ASME J. Heat Transfer, **108**, pp. 597–601.

[11] Hoadley, A. F. A., Pappoz, M., and Zimmermann, M., 1991, "Heat-Flow Simulation of Laser Remelting With Experimental Validation," Metall. Trans. B, **22B**, pp. 101–109.

[12] Hecter, Jr., L. G., Kim, W. S., and Drisik, M. N., 1992, "Hyperbolic Heat Conduction due to a Mode Locked Laser Pulse Train," Int. J. Eng. Sci., **30**, pp. 1731–1744.

[13] Ashfort-Frost, S., and Jamburnathran, P., 1996, "Numerical Prediction of Semi-confined Jet Impingement and Comparisons With Experimental Data," Int. J. Numer. Methods Fluids, **23**, pp. 295–306.

[14] Ariel, P. D., 1993, "Stagnation Flow—A Free Boundary Value Problem Formulation," Int. J. Comput. Math., **49**, pp. 123–131.

[15] Abid, R., and Speziale, C. G., 1996, "The Free Stream Matching Condition for Stagnation Point Turbulent Flows: An Alternative Formulation," ASME J. Appl. Mech., **63**, pp. 95–100.

[16] Craft, T. S., Graham, L. J. W., and Launder, B. E., 1993, "Impinging Jet Studies for Turbulence Model Assessment-II. An Examination of the Performance of Few Turbulence Models," Int. J. Heat Mass Transf., **36**, pp. 2685–2697.

[17] Strahle, W. C., 1985, "Stagnation Point Flows With Freestream Turbulence—The Matching Condition," AIAA J., **23**, pp. 1822–1824.

[18] Shuja, S. Z., and Yilbas, B. S., 1998, "Gas-Assisted Repetitive Pulsed Heating of a Steel Surface," Proc. Inst. Mech. Eng., Part C: J. Mech. Eng. Sci., **212**, pp. 741–757.

[19] Shuja, S. Z., and Yilbas, B. S., 1998, "Pulsative Heating of Surfaces," Int. J. Heat Mass Transf., **41**, pp. 3899–3918.

[20] Chu, J. P., Rigsbee, J. M., Banons, G., and Elsayed-Ali, H. E., 1999, "Laser Shock Processing Effects on Surface Microstructure and Mechanical Properties of Low Carbon Steel," Mater. Sci. Eng., A, **260**, pp. 260–268.

[21] Hasselmon, D. P. H., and Crandall, W. B., 1963, "Thermal Shock Analysis of Spherical Shapes-II," J. Am. Ceram. Soc., **49**, pp. 434–437.

[22] Wang, H. G., Guan, Y. H., Chen, T. L., and Zhang, J. T., 1997, "A Study of Thermal Stresses During Laser Quenching," J. Mater. Process. Technol., **63**, pp. 550–553.

[23] Modest, M. F., 1998, "Transient Elastic and Viscoelastic Thermal Stresses During Laser Drilling of Ceramics," ASME J. Heat Transfer, **120**, pp. 892–898.

[24] Dain, Y., Kapadia, P. D., and Dowden, J. M., 1999, "The Distortion Gap Width and Stresses in Laser Welding of Thin Elastic Plates," J. Phys. D, **32**, pp. 168–175.

[25] Elperin, T., and Rudin, G., 1996, "Thermoelasticity Problem for a Multilayer Coating-Substrate Assembly Irradiated by a Laser Beam," Int. Commun. Heat Mass Transfer, **23**, pp. 133–142.

[26] Li, K., and Sheng, P., 1995, "Plane Stress Model for Fracture of Ceramics During Laser Cutting," Int. J. Mach. Tools Manuf., **35**, pp. 1493–1506.

[27] Yilbas, B. S., Sami, M., and Shuja, S. Z., 1998, "Laser-Induced Thermal Stresses on Steel Surface," Opt. Lasers Eng., **30**, pp. 25–37.

[28] Berocci, C., 1991, *Introduction to the Modeling of Turbulence*, Von Karman Inst for Fluid Dynamics, March.

[29] Gotski, T. B., Hussaini, M. Y., and Lumley J. L., 1996, *Simulation and Modeling of Turbulent Flows*, Oxford Univ. Press, New York.

[30] Elhaleim, O., Reggio, M., and Camatero, R., 1992, "Simulating Two-Dimensional Turbulent Flow by Using $k-\varepsilon$ Model and the Vorticity-Stream Function Formulation," Int. J. Numer. Methods Fluids, **14**, pp. 961–980.

[31] Incropera, F. P., and Dewitt, D. P., 1985, *Introduction to Heat Transfer*, Appendix, John Wiley, New York, pp. 667–696.

[32] Patankar, S. V., 1981, *Computer Analysis of Fluid Flow and Heat Transfer*, Ch.8, Pinridge, Swansea, pp. 223–252.

[33] Shuja, S. Z., 1993, "Calculations of Fluid Flow and Heat Transfer in Expanding Ducts," MS Thesis, King Fahd Univ., Dhahran, Saudi Arabia.

[34] Bathe, K. J., 1996, *Finite Element Procedures*, Ch.6, Prentice Hall, New Jersey, pp. 148–192.